



ELSEVIER

Deep-Sea Research II 51 (2004) 2995–3008

DEEP-SEA RESEARCH
PART II

www.elsevier.com/locate/dsr2

Internal tides in the Bay of Biscay: conversion rates and seasonal effects

Theo Gerkema^{a,*}, Frans-Peter A. Lam^{b,2}, Leo R.M. Maas^b

^aLaboratoire des Ecoulements Géophysiques et Industriels (LEGI), BP 53, 38041 Grenoble Cedex 9, France

^bRoyal Netherlands Institute for Sea Research (NIOZ), P.O. Box 59, 1790 AB Texel, The Netherlands

Abstract

Internal tides in the Bay of Biscay are studied using a numerical linear hydrostatic internal-tide generation model, in which along-slope uniformity is assumed. The focus is on the seasonal changes in the generation and dynamics. The results are compared with observations made near the shelf-break in early summer. They were obtained using a towed Acoustic Doppler Current Profiler (ADCP) on repeated tracks in the Bay of Biscay; this provides a synoptic view in a plane spanned by the vertical and the cross-slope direction. In the reproduction of the observed patterns by the numerical model, the presence of the seasonal thermocline turns out to be essential. However, the model results also indicate that its presence has only a minor effect on the integrated conversion rate (which is about 10 kW/m). The main region of generation lies deep and is seasonally independent; the presence of the deep permanent pycnocline does increase the integrated conversion rate strongly, by a factor two.

© 2004 Elsevier Ltd. All rights reserved.

1. Introduction

The Bay of Biscay is thought to offer one of the world's strongest generation sites for internal tides. For this region, Baines (1982) obtained a relatively high estimate of the conversion rate (from

barotropic into baroclinic tides), and Pingree and New (1991) observed a distinct internal-tide beam, in which vertical displacements were as large as 300 m (peak-to-trough).

Baines' analysis yielded estimates of conversion rates along continental slopes worldwide; they were later complemented by Morozov (1995) for deep-ocean ridges. Munk (1997) argued that the two-dimensionality assumed in the analysis of Baines (1982) is too restrictive, and that three-dimensional features like canyons are likely to contribute significantly. This presumes that the along-slope barotropic tidal flux is much stronger than the across-slope one, which is however not

*Corresponding author.

E-mail address: gerk@nioz.nl (T. Gerkema).

¹Present affiliation: Royal Netherlands Institute for Sea Research (NIOZ), P.O. Box 59, 1790 AB Texel, The Netherlands.

²Present affiliation: TNO Physics and Electronics Laboratory (TNO-FEL), Underwater Acoustics Department, P.O. Box 96864, 2509 JG The Hague, The Netherlands.

the case in the Bay of Biscay (LeCann, 1990; Lam et al., 2004). Yet, even in a purely two-dimensional setting there is ample room for reconsidering Baines' estimates. For example, Baines (1982) adopted a linear slope; as a consequence, the forcing is concentrated at the shelf-break, and the conversion rate shows a strong seasonal dependence. For a more realistic topography, the region of strong forcing (conversion) will be extended, or even shifted, to deeper positions. One must expect that the effect of seasonality loses importance as the deeper (and seasonally independent) generation gains importance. We will argue below that Baines (1982) probably overestimated the conversion rate in the seasonal thermocline, while underestimating the conversion rate in the deep continuously stratified layer. A correction of the latter diminishes the importance of seasonality, and increases the overall conversion rate.

Baines (1982) included seasonal effects by separating the interfacial tide from the tidal beam. The interfacial tide is associated with the seasonal thermocline, which he represented by a δ -function in N^2 (N the buoyancy frequency); the tidal beam is associated with the much weaker deep stratification, which he represented by a layer of constant N . As Baines points out, such a separation is possible if the thermocline is sufficiently strong, because in that case a distinct interfacial mode exists (the first mode), while all higher modes combine to form the beam below the thermocline. It was suggested in Gerkema (2001) that the thermocline in the Bay of Biscay may in fact not be sufficiently strong, implying that no distinct interfacial mode exists, and resulting in a hybrid beam-interfacial manifestation of the internal tide. This will be confirmed below.

Looked upon in terms of ray-theory, instead of a modal decomposition, this hybrid behaviour can be interpreted as a scattering of the beam, the second theme of this paper. Some explanation of this usage of the word 'scattering' may be appropriate. Internal tides, and internal waves in general, owe their existence to the stratification, a measure of which is N . Variations in $N(z)$ affect the propagation of internal waves in two ways. First, it makes the direction of energy propagation vary (refraction), according to $\tan^2 \theta = (N^2(z) -$

$\sigma^2)/(\sigma^2 - f^2)$, where θ denotes the angle between the direction of energy-propagation and the vertical z . Here, σ is the tidal frequency, and f the Coriolis parameter. As long as N varies weakly on the typical vertical scale of the internal wave, this will be the sole effect. For more strongly varying N , a second effect comes into play: internal reflections, also called secondary reflections (Brekhovskikh, 1960). Multiple secondary reflections cause an initially confined beam to spread: its energy gets scattered over a wide area, but with relatively much energy staying in the thermocline and the mixed layer (as we shall illustrate below). For a very strong thin thermocline, finally, the beam would simply reflect at it, like at a rigid surface, and no significant scattering would occur (this is the regime in which a distinct interfacial mode exists). These processes were studied analytically in a simple setting in Gerkema (2001), where the stratification model of Baines (1982) was adopted. In this paper, the occurrence of scattering will be studied for a more realistic profile of N and topography, by using a numerical model. Since the scattering occurs predominantly in the seasonal thermocline, the seasonal character of scattering is clear a priori, and will indeed be confirmed in this paper.

The outline is as follows. First we present ADCP-observations obtained near the shelf-break during early summer (Section 2.1). The results are compared with those of an internal-tide generation model; model results for winter stratification are also presented (Section 2.2). Next we consider the model results concerning energy-density and conversion rates in the shelf-break region, and compare summer and winter conditions (Section 3). In this section we also reconsider the earlier estimates obtained by Baines (1982). Finally, we show the model results for the far-field (the central Bay of Biscay), and discuss the effects of scattering of a beam at the seasonal thermocline (Section 4).

2. The generation region—current fields

To check whether the model yields realistic results, we compare its outcome with observations

on internal-tide currents, obtained near the shelf-break, which are briefly described below.

2.1. Observations

From 4 to 8 June 1993 three cross-isobath transects, about 35 km apart and 13 km long, were monitored over the shelf-break in the Bay of Biscay (see Fig. 1), each for about 1 day, as part of the *Triple B '93* project (Van Aken, 1995). A downward-looking narrowband 75 kHz ADCP was towed by the ship, measuring the three-dimensional currents from 10 m below the water surface to the sea floor in ‘bins’ with a thickness of 8 m. The tracks were repeated, and thus each position on the track was visited at least 10 times. This allows one to fit a sinusoidal tidal signal to each bin; in the fit, an additive constant represents

the residual signal. More details on the observational techniques and on the analysis of the signal, including results on the barotropic tidal currents, are presented elsewhere (Lam et al., 2004). Here we focus on the baroclinic tidal signal, which we obtain (approximately) by subtracting the depth-averaged signal; examples of depth-averaged tidal ellipses are shown in Fig. 1.

At each position the fitted baroclinic tidal signal of the cross-slope component can be written as

$$u = A(x, z) \sin[\sigma t - \phi(x, z)], \tag{1}$$

thus lines of equal phase propagate in the direction of increasing ϕ . The resulting amplitude A and phase ϕ for one transect (the other two are similar) are shown in Fig. 2. A number of conspicuous features is revealed in these observations. First of all, the distinctive blue band in Fig. 2A, where

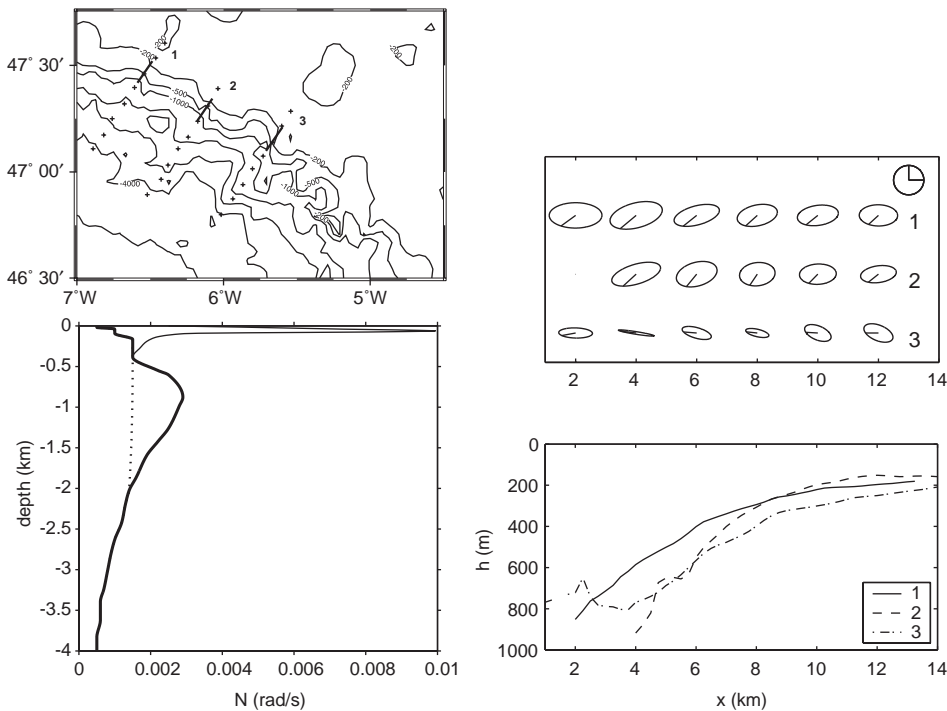


Fig. 1. Left-hand panels: bathymetry and transects where ADCP measurements were made (the results of transect 1 are used in this paper); and (lower panel) the stratification profiles used in the model calculations: summer (thin line), winter (thick line), and a fictitious ‘winter’ profile in which the permanent pycnocline has been removed (dots). Right-hand panels: barotropic tidal ellipses (in terms of transport) over each of the transects (topography is shown in the lower panel); the horizontal axis of the ellipse gives the cross-slope transport, the vertical axis the along-slope transport; notice that the former exceeds the latter in all cases. The radius in the reference circle indicates a flux of $100 \text{ m}^2 \text{ s}^{-1}$.

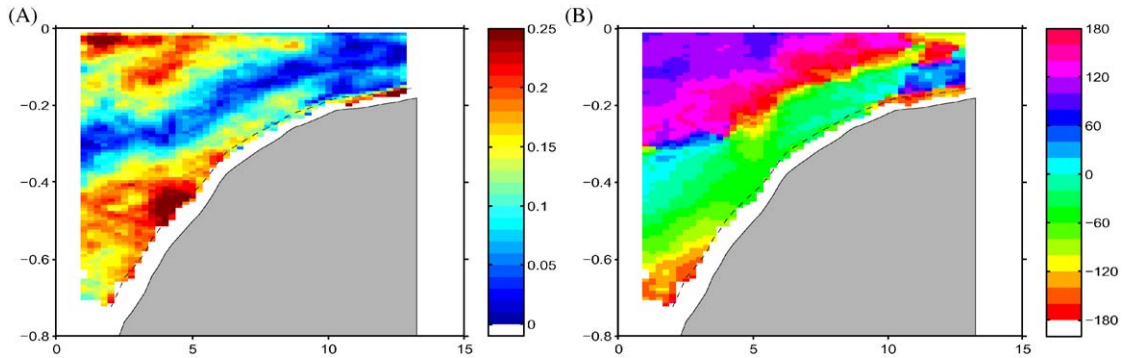


Fig. 2. Results from ADCP observations in the Bay of Biscay ($x = 0$: 47.42°N; 6.59°W): the baroclinic cross-slope tidal current, decomposed in (A) its amplitude (in m s^{-1}) and (B) its phase (in degrees). Distances along the axes are in km. The x -axis is directed 34.2° True North.

currents are zero, or nearly so; it runs from the middle left to the upper right, and divides the figure into two parts. In this band, an amphidromic point occurs near $x = 4.5$ km, $z = -270$ m. By an amphidromic point we understand a position at which the currents vanish while co-phase lines circle around it. In the context of internal tides, this phenomenon was first identified by DeWitt et al. (1986). To the left of this point, phase propagation is generally upward (except in the upper 150 m); to the right, it is generally downward (Fig. 2B).

In particular, in the region at the lower left (i.e. below the blue band), where currents are particularly strong, phase propagation is upward. Basic results from internal-wave theory indicate that the group-velocity (i.e. the direction of energy-propagation) is perpendicular to the direction of phase-propagation (i.e. parallel to co-phase lines), with opposing vertical components (LeBlond and Mysak, 1978). Applying these theoretical results, we find that internal-tide energy propagates downward in this region, parallel to the co-phase lines. As we shall discuss below, this signal in fact belongs to the most upper part of an internal-tide beam similar to the one observed by Pingree and New (1991), further off the shelf-break.

The region in the upper left corner (i.e. above the blue band) also shows strong currents, but the direction of phase propagation is less distinctive.

With the use of the numerical model, we shall suggest an interpretation of this phenomenon.

2.2. Model results

In this study we use a linear hydrostatic internal-tide generation model. It is a slightly modified version of the model described in Gerkema (2002); a more accurate numerical scheme is now used (see below). The model can be employed for arbitrary stratification $N(z)$ and topography $z = h(x)$ (x is the across-slope direction, z the vertical). Uniformity is assumed in the along-slope direction: $\partial/\partial y = 0$.

2.2.1. Model equations

We use the inviscid linear hydrostatic equations on the f -plane, under the Boussinesq approximation (partial derivatives are denoted by indices):

$$\psi_{zzt} - f v_z + b_x = 0, \quad (2)$$

$$v_t + f \psi_z = 0, \quad (3)$$

$$b_t - N^2 \psi_x = -N^2 W. \quad (4)$$

Here ψ is the streamfunction ($u = \psi_z$, $w = -\psi_x$); v the along-slope velocity component; b denotes buoyancy, defined as ‘minus effective gravity’: $b = -g\rho/\rho_*$, where ρ is the density’s local departure from its hydrostatic value, and ρ_* a constant reference value of density. Isopycnal displacements (ζ) can be derived from buoyancy via $b = -N^2\zeta$.

For the stream function we impose the boundary conditions $\psi = 0$ at bottom and surface (rigid-lid).

The barotropic forcing is prescribed via W , the vertical velocity component of the barotropic tide, an expression of which is obtained in the following way. We assume that the cross-slope barotropic tidal flow U is such that it produces a spatially constant but time-oscillating flux: $U(t, x)h(x) = Q_0 \sin \sigma t$ (constant Q_0). Via continuity, $U_x + W_z = 0$, we then find for W :

$$W = z \frac{Q_0 \sin \sigma t}{h(x)^2} h_x, \quad (5)$$

where the integration constant was chosen such that $W|_{z=0} = 0$.

The model equations do not only produce time-oscillating fields, but also mean fields for b and v , depending on the initial conditions. This can be seen as follows: (3) and (4) imply

$$v_x + f \left(\frac{b}{N^2} \right)_z = f \frac{Q_0 \cos \sigma t}{\sigma h^2} h_x + c(x, z), \quad (6)$$

where $c(x, z)$ is a ‘constant’ of integration due to time-integration. This constant will be nonzero if we choose (as is natural) $v = b = 0$ at $t = 0$; as a consequence, v and b will then contain stationary fields at later times. These fields form an arbitrary and artificial element in the solution, since they depend on how we choose the initial conditions. They reflect the ‘memory’ of the system over the topography due to Coriolis effects, and (6) can in fact be interpreted as an expression of conservation of potential vorticity. As expected, we found that the stationary fields become negligible if we replace $\sin \sigma t$ in (5) by $\cos \sigma t$ (giving $\sin \sigma t$ in (6)), but this abrupt way of starting the forcing will usually be less attractive from a numerical point of view.

2.2.2. Numerical scheme and resolution

A new vertical coordinate is introduced: $\eta = 1 - 2z/h(x)$, which transforms the vertical domain to $(-1, 1)$. The Eqs. (2)–(5) are transformed accordingly. The boundary conditions then become $\psi = 0$ at $\eta = \pm 1$. In the vertical, a Chebyshev collocation method is used, the collocation points being defined by $\eta_k = \cos(\pi(k-1)/(K-1))$ for $k = 1, \dots, K$. This gives a higher resolution

near the surface (and bottom), which improves the resolution in the seasonal thermocline and the description of the reflection of beams at surface and bottom.

We use central differences in x (5-point symmetric, 4th-order), and perform the time-integration using a third-order Adams–Bashforth scheme. A fourth-order spatial filter is used to selectively dampen oscillations on the grid scale (Durrant, 1999). Sponge layers are used by including Rayleigh friction, the frictional coefficient being zero at the entrance of the sponge, and increasing linearly inward. The thickness of the sponge is 150 km in the deep ocean, and 50 km on the shelf.

In all calculations shown below (except those in Section 3.1) the horizontal step is 400 m; this means that the continental slope is covered by some 100 points. In the vertical a sufficiently good resolution is obtained by using 80 collocation points. The number of time steps per tidal period (M2) is 800, giving a time step of nearly 56 s. Each run spans 60 tidal periods; this length is sufficient to ensure that all transients have left the domain under consideration by the end of the run. The results we show are taken from the last period.

2.2.3. Results

For the stratification we use an observed profile (Fig. 1, thin line), in which a pronounced seasonal thermocline is present. We also do calculations for a winter profile, in which the thermocline has been removed (thick line). In both profiles a clear permanent pycnocline is present (around 1 km depth), which is typical of the Bay of Biscay (Van Aken, 2001). In one model calculation (next section), we use a fictitious profile in which the permanent pycnocline has been removed as well (dotted line in Fig. 1). For the topography we use data from an observed nearby transect traversed in a later cruise, which covered the whole slope. For Q_0 , the amplitude of the barotropic cross-slope flux, we choose $100 \text{ m}^2 \text{ s}^{-1}$, being a typical value for this region (see Fig. 1).

We present the results in terms of the cross-slope baroclinic current u , decomposed into amplitude and phase fields as in (1), see Fig. 3. To facilitate the interpretation, a larger domain is shown than in the observations; the observational domain is

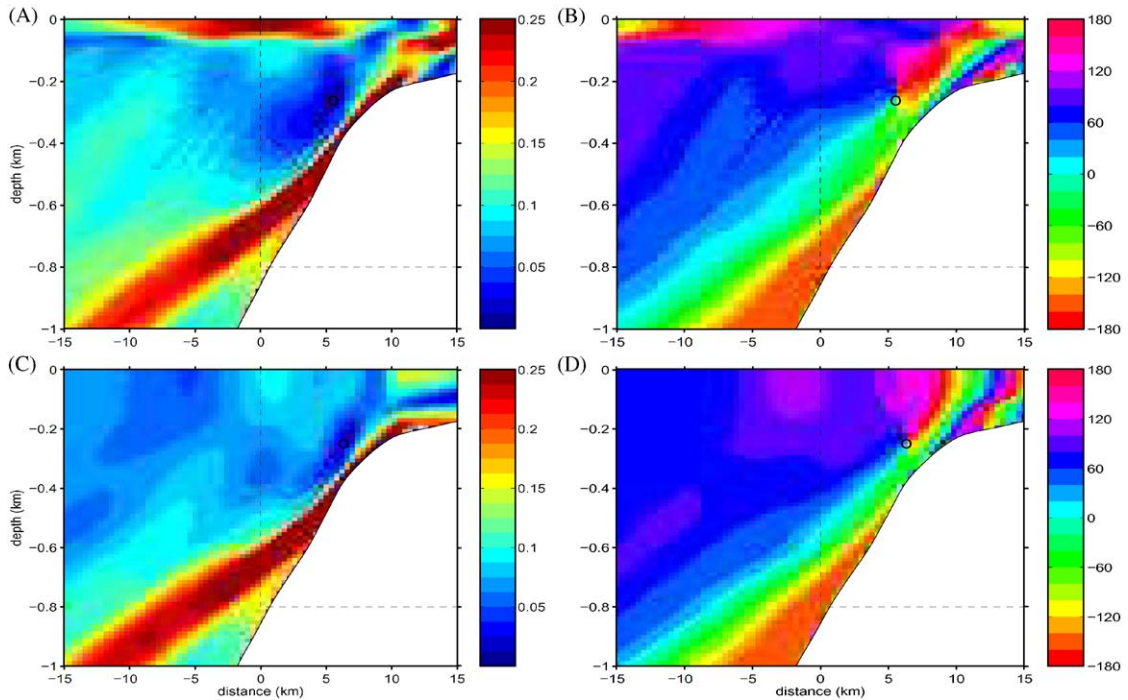


Fig. 3. Model results: the baroclinic cross-slope component ($u = \psi_z$), decomposed into: (A, C) amplitude A (in m s^{-1}); (B, D) phase ϕ (in degrees), for two different stratifications: (A, B) summer; (C, D) winter. The box delineates the region of observation, see Fig. 2. The circles indicate the presence of an amphidromic point.

indicated by a box. In Figs. 3A and B the results are shown for the observed (summer) stratification. The model reproduces the diagonal blue band of near-zero currents, the small region of strong currents in the upper-left part, and the strong currents in the lower-left part, initially attached to the topography. Also the amphidromic point is well reproduced, although not exactly at the same location: $x = 5.6 \text{ km}$, $z = -250 \text{ m}$ (see circles), which is more to the right, and slightly higher, than in the observations. The strong tidal currents in the lower-left part are (as in the observations) associated with upward phase propagation, hence downward energy propagation along the co-phase lines; the beam-like nature is clearly seen in Fig. 3A. In the upper-left part, the direction of phase propagation is unclear, like in the observations.

Finally, at the right-end of the domain, the internal tides propagate on-shelf. There the pattern corresponds less well with that of the

observations. This might be due to barotropic advection (neglected in the model), which can be expected to become significant in shallow regions in that it affects the propagation of the internal tide (modifying its effective phase speed), as was observed by Pingree et al. (1986). Another cause of the difference may lie in horizontal changes in stratification on the shelf-side. Since the focus of this paper is on the internal tides travelling into the deep ocean, we shall not pursue this problem here.

For completeness, we also present the results for winter stratification (no seasonal thermocline, see Fig. 1), all other parameters being the same. In this case, we have no observations to compare with. In the upper 200 m, the pattern (see Figs. 3C and D) looks very different from that during summer. Only the strong currents in the deep lower-left part have ‘survived’ the removal of the seasonal thermocline, and form (as in Fig. 3A) the beginning of a distinct beam that propagates into the abyssal ocean. In the rest of this paper, we shall

refer to this beam as the *main beam*; it is equally present in summer and winter.

3. The generation region—conversion rates

From (2) to (4) one can derive the following energy equation:

$$E_t + \rho_* [f(\psi v)_z - (\psi \psi_{zt})_z - (\psi b)_x] = -\rho_* b W, \quad (7)$$

where E denotes the energy-density:

$$E = \frac{1}{2} \rho_* \{(\psi_z)^2 + v^2 + b^2/N^2\}. \quad (8)$$

The term $\rho_*[\cdot \cdot \cdot]$ on the left-hand side of (7) can also be written in the familiar flux-form $\nabla \cdot (p\vec{u})$, where p is the baroclinic pressure. For a purely time-periodic signal, the first term on the left-hand side (7) yields zero if we integrate over one tidal period T , hence

$$\rho_* \langle f(\psi v)_z - (\psi \psi_{zt})_z - (\psi b)_x \rangle = -\rho_* \langle b W \rangle, \quad (9)$$

where $\langle \cdot \rangle = T^{-1} \int_0^T dt$. We define

$$C = -\rho_* \langle b W \rangle \quad (10)$$

as the local *conversion rate*; C indicates how much energy per second per unit volume is converted from barotropic into baroclinic tides. Notice that one cannot calculate C a priori, because it contains the baroclinic field b , which first has to be solved from the model equations. This reflects the fact that the amount of energy converted at some locations depends not only on the local forcing (W) but also on the signal produced elsewhere.

The isopycnal displacement ζ (and also the buoyancy, b) includes the purely barotropically induced vertical elevations (over the topography). These elevations correctly give no contribution to the right-hand side of (10), because the corresponding b and W are 90° out of phase. The artificial mean fields discussed in Section 2.2.1 give no contribution, either. This can be seen by writing $b = \tilde{b}(x, z) + b'(t, x, z)$, where \tilde{b} denotes the mean field, while b' is purely oscillatory. Now, \tilde{b} obviously leaves the conversion rate C unaffected, and it does not modify b' either (which would indirectly affect C), since the model is linear. Thus, the arbitrariness in the solution does, fortunately, not extend to the important quantity C . However,

the mean fields \tilde{b} can be expected to disturb C in nonlinear models, for we found that \tilde{b} is relatively large in the main region of generation; the outcome of conversion rates in nonlinear models should therefore be regarded with caution.

In view of the two-dimensionality of our problem, we define the ‘integrated conversion rate’ C_{int} as the integral of C over the xz -plane, being equivalent to the ‘total energy flux’ in Baines (1982). The equivalence becomes clear if we integrate (9) over the horizontal domain (x_1, x_2) , covering the entire generation region, and over the vertical domain $(h(x), 0)$:

$$-\rho_* \left(\int dz \langle \psi b \rangle \right) \Big|_{x_1}^{x_2} = \int dx \int dz C \equiv C_{\text{int}}. \quad (11)$$

The expression on the left-hand side is also useful in determining the integrated conversion rate empirically, since $b = -N^2\zeta$ and ψ are relatively easy to obtain.

Before showing the results for C and C_{int} for the region of observation (Section 3.2), we first consider the idealized case of a linear slope to place our estimates in the context of those obtained before.

3.1. Linear slopes: comparison with earlier estimates

Recent analytical studies on the conversion rate were made by Llewellynn Smith and Young (2002) and Khatiwala (2003), under the assumption of infinitesimal topography. (Notice that Llewellynn Smith and Young (2002) understand by the ‘conversion rate’ the quantity C as above, but integrated over all three spatial directions.) For continental slopes, i.e. finite-amplitude topography, an analytical result is known for the special case of a step-topography. A solution was derived by Sjöberg and Stigebrandt (1992), who however neglected the on-shelf propagating internal tide. Their solution has recently been generalized to include the on-shelf contribution as well (St. Laurent et al., 2003; Sanchis, 2003).

For linear slopes other than a step no closed expression has been obtained so far. In a semi-analytical approach, Baines (1982) obtained

estimates for the conversion rates in the seasonal thermocline (interfacial tides) and in the constantly stratified deep layer beneath it (internal-tide beams). For the Bay of Biscay, he found 0.936 and 0.232 kW m^{-1} , respectively, implying that seasonality is a dominant factor in the conversion rates. However, the latter value deserves further scrutiny; we shall reconsider it in isolation by momentarily ignoring the seasonal thermocline.

We have done a series of calculations, using the following parameters: latitude 45°N , constant buoyancy frequency $N = 5.5 \times 10^{-3} \text{ rad s}^{-1}$, shelf depth 135 m , ocean depth 4 km , M2 tidal-frequency $\sigma = 1.405 \times 10^{-4} \text{ rad s}^{-1}$, $\rho_* = 1025 \text{ kg m}^{-3}$. These values correspond essentially to those used by Baines (1982), except that we have ignored the mixed layer of 100 m thickness, which he included by taking $N = 0$ there (see below). Two crucially important parameters, however, were not specified: the cross-slope barotropic flux Q_0 and the slope length L . For the former we take $100 \text{ m}^2 \text{ s}^{-1}$, and we will vary L from 10 to 50 km . In treating the generation at a linear slope numerically, one does not easily find accurate values of the integrated conversion rate (and proper convergence for finer resolution), because the conversion is largely concentrated at the sharp upper corner of the slope. We have therefore replaced the corner, over an interval 2ε , by a parabolic profile such that h becomes continuously differentiable (we have similarly replaced the corner at the foot of the slope). This is a mathematically consistent way of smoothing, since the second derivative of h is now piecewise constant and properly yields two δ -distributions in the limit $\varepsilon \rightarrow 0$. We chose $\varepsilon = 2 \text{ km}$; we used 100 collocation points in the vertical, a horizontal step of 100 m , and 4000 time steps per tidal period (six tidal periods in total).

The results are gathered in Fig. 4; they allow us to draw three conclusions. First, in this regime of steep slopes, the value of C_{int} varies little with slope length L , and is always close to the theoretical value for a step (St. Laurent et al., 2003), indicated by the horizontal dotted line (36.6 kW m^{-1}). Second, the values for C_{int} in Fig. 4 are *two* orders of magnitude larger than Baines' (which was 0.232 kW m^{-1}). Third, the preceding two points imply that the discrepancy cannot be

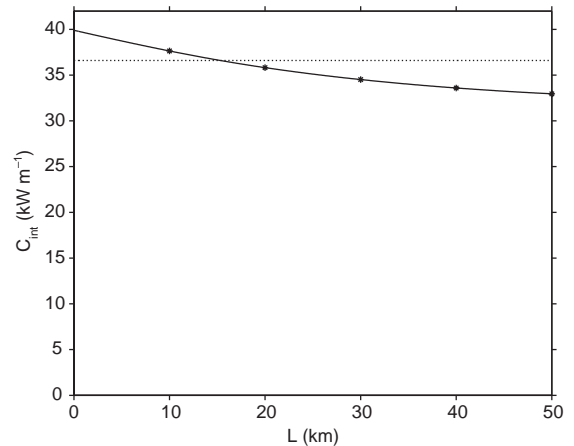


Fig. 4. The integrated conversion rate C_{int} as a function of slope length L , for near-linear slopes (points); the solid line results from a cubic interpolation (and extrapolation for $L < 10 \text{ km}$), and the horizontal dotted line represents the theoretical exact value for a step-topography.

ascribed to a possible difference in the value of L . Furthermore, we found that adding a mixed layer of 100 m thickness (as had Baines) reduces C_{int} only by about 2%.

If we assume that Baines' estimate is technically accurate (we notice, however, that his derivation involves a few approximations), then the explanation of the discrepancy must stem from a difference in the choice of the barotropic cross-slope flux, Q_0 . Our value of $100 \text{ m}^2 \text{ s}^{-1}$, although appropriate for the region we consider (see Fig. 1), is indeed not representative for the Bay of Biscay as a whole. However, to arrive at Baines' value for C_{int} , we would have to reduce Q_0 by a factor of ten (since C_{int} is proportional to Q_0^2), giving an unrealistically small Q_0 . Judging from observations and calculations made by LeCann (1990), we may conclude that a representative value is $Q_0 = 30 - 40 \text{ m}^2 \text{ s}^{-1}$; this would reduce the value for C_{int} from Fig. 4 by one order of magnitude, leaving it still *one* order of magnitude higher than Baines'. (As an aside, we notice that Fig. 7B in LeCann (1990), like our Fig. 1, demonstrates clearly that cross-slope fluxes are generally larger than along-slope fluxes.)

Although questions remain, it seems safe to conclude that Baines' estimate of the contribution

of the continuously stratified deep layer to C_{int} is too small by one order of magnitude.

3.2. Results

We now return to the model results for the Bay of Biscay for the observed topography and stratification. In Fig. 5 we show the tidal-averaged energy density (E), and the conversion rate C , both for summer and winter. C_{int} , the integrated value of C , is also indicated in the figures. As mentioned above, the integration is made over the xz -plane, so that the resulting quantity is in Watt per meter, which can be interpreted as Watt per unit slope-length (in the transverse direction, y). During summer, one can identify two well-separated source regions (Fig. 5B): a relatively deep one, attached to the slope, and a small region higher up, which lies in the seasonal thermocline. The latter is indeed absent during winter (Fig. 5D).

It is now clear that the seasonal thermocline forms the source-region of the strong internal-tide currents in the upper-layer on the left as well as of the on-shelf propagating internal tides (Fig. 2A, Fig. 3A); both are absent during winter (Fig. 3C). Although the baroclinic fields look very different in summer and winter, notably in the upper 200 m (Figs. 5A and C), the integrated conversion rates C_{int} are fairly comparable (Figs. 5B and D); during winter, its value is only 15% smaller. In other words, the model indicates that the manifestation of internal tides is very different in summer and winter, while their total energy is not. Figs. 5B and D show clearly why there is little seasonal dependence in C_{int} : the main region of energy conversion lies well below the seasonal thermocline; it is also the region from which the main beam originates.

The values for C_{int} obtained here lie still remarkably close to the value for the step-topography

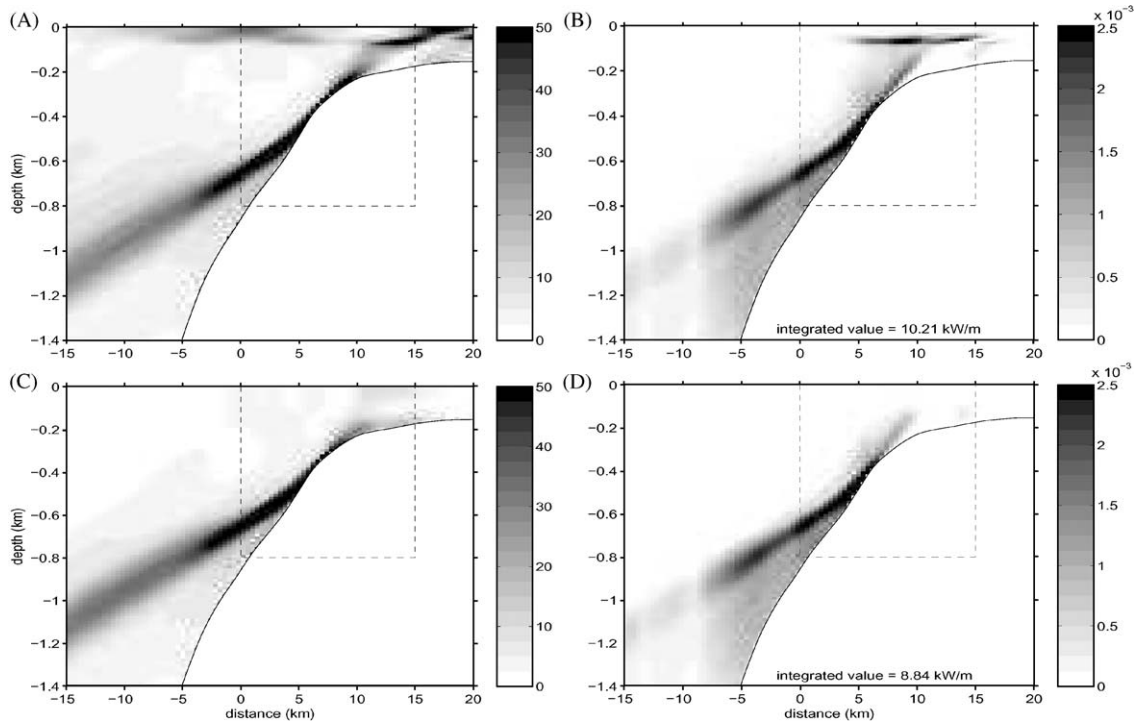


Fig. 5. Model results: (A) the tidal-averaged baroclinic energy-density (E) (in J m^{-3}) during summer; (B) the conversion rate C (in W m^{-3}) during summer; (C) E during winter; (D) C during winter. The box delineates the region of observation. In (B, D) the integrated value over the xz -plane, C_{int} , is also indicated.

and near-linear slopes of Fig. 4, if we allow for the fact that in the main region of generation (see Fig. 5D), N is about two to three times smaller than the value used in Fig. 4. (For a step-topography, C_{int} becomes proportional to N under the hydrostatic approximation, see St. Laurent et al., 2003).

The difference we find between summer and winter (1.36 kW m^{-1}), which can be ascribed to the seasonal thermocline, is of the same order of magnitude as the contribution Baines (1982) found for the seasonal thermocline (0.936 kW m^{-1}). This is remarkable in view of our conclusion, argued above, that Baines probably used a much lower value for the barotropic cross-slope flux, Q_0 . However, this will be compensated (at least in part) by the fact that he used a linear slope; the position of maximum W is then located at the upper corner of the slope, which lies close to the seasonal thermocline. For a realistic topography, W takes its maximum value at a much deeper position.

Finally, we consider a fictitious stratification in which the permanent pycnocline has been removed as well (Fig. 1, dotted line). The results (Fig. 6) are qualitatively similar to those during winter, except that the main (and only) beam is now steeper near 1 km depth, due to the decreased value of N . However, quantitatively there is a very significant difference: the integrated conversion rate has been halved, compared to the winter situation. This means that the permanent pycnocline is of primary

importance for a correct modeling of the energetics and conversion rates.

4. The far field—scattering

We now consider the development of the internal tides as they propagate further into the deep ocean. To this end, we show the baroclinic cross-slope component u (again decomposed in amplitude and phase fields as in (1)), both for summer and winter, see Fig. 7.

The interpretation of the results during winter is most straightforward (Figs. 7C and D): here the main beam is the only beam present. It originates from the upper parts of the slope (cf. Figs. 5C and D), and first moves downward, then reflects at the bottom ($x = -55 \text{ km}$), and later at the surface ($x = -120 \text{ km}$). The beam is less intense (less narrow) after its reflection at the bottom than before; this is because the bottom is sloping, and hence defocuses the beam. The direction of the beam changes slightly with the vertical (steeper at deeper positions), which is due to the varying stratification; this is the refraction discussed in Section 1. Essentially, it amounts to a WKB-like adaptation to a weakly varying background field, $N(z)$; no significant scattering occurs. In Fig. 7C we have added the positions at which Pingree and New (1991) found the maximum vertical displacements (see their Fig. 9). Although their

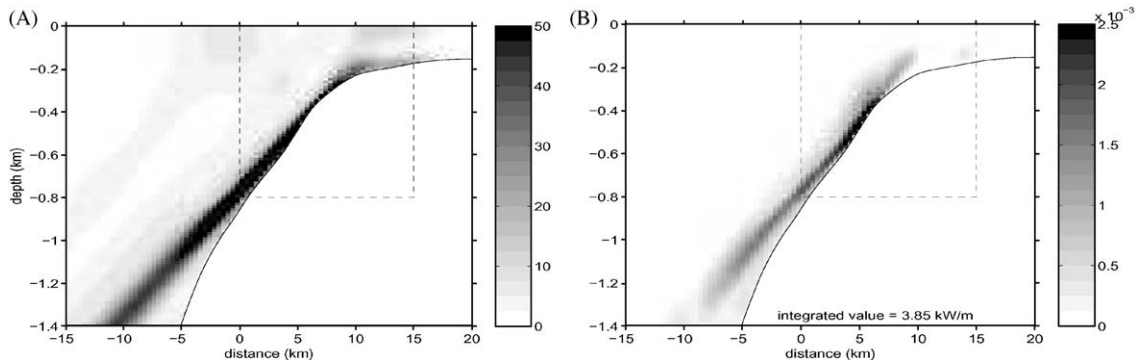


Fig. 6. Model results for a fictitious profile of N , in which the permanent pycnocline has been removed: (A) the tidal-averaged baroclinic energy-density (E) (in J m^{-3}); (B) the conversion rate C (in W m^{-3}). The box delineates the region of observation. In (B) the integrated value over the xz -plane, C_{int} , is also indicated.

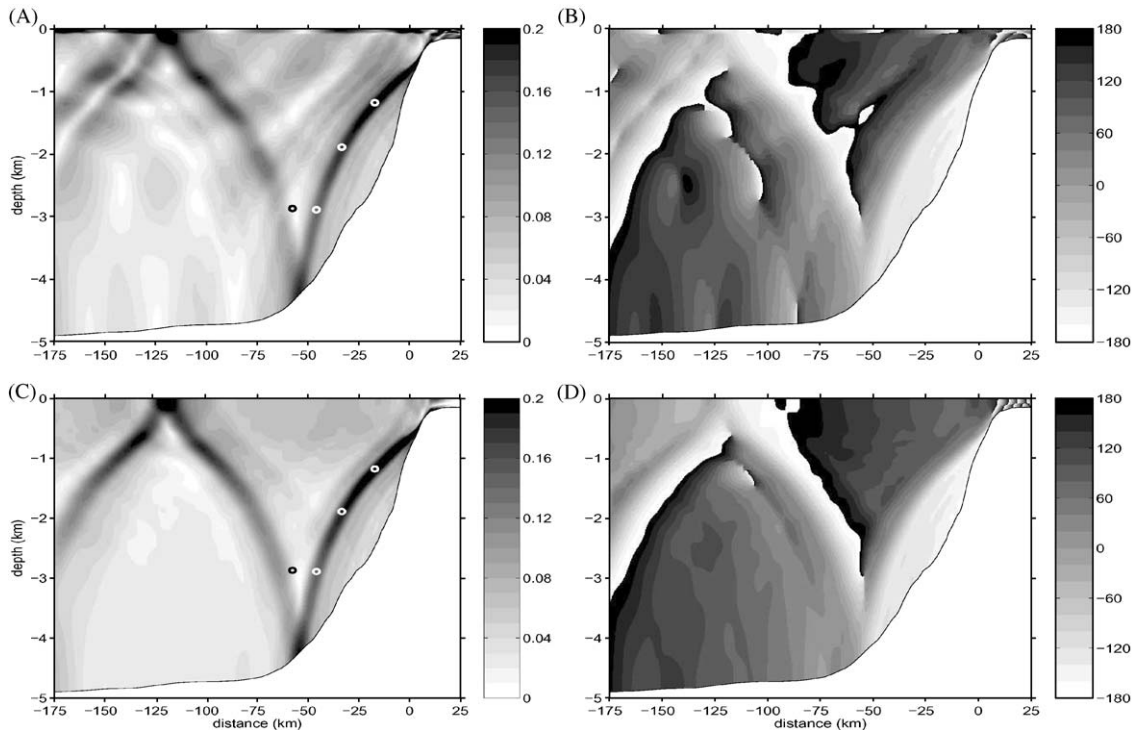


Fig. 7. Model results, large domain: the baroclinic cross-slope component ($u = \psi_z$), decomposed into: (A, C) amplitude A (in m s^{-1}); and (B, D) phase ϕ (in degrees; notice that the extremes of black and white denote the same phase), for two different stratifications: (A, B) summer; (C, D) winter. The circles indicate the location of the main beam as observed by Pingree and New (1991).

measurements were made during summer, one expects no seasonal effects in the beam's initial downward propagation, given the depth of the generation region; the correspondence is indeed very satisfactory.

During summer, the manifestation of internal tides is very different: see Figs. 7A and B. The only part that remains the same as during winter is the initial downward path of the main beam. Above this beam, and parallel to it, one now discerns weak beams (in grey), which originate from the regions in the thermocline/mixed-layer where currents are strong: i.e. near $x = 0, -35$ and -70 km. They interfere with the main beam, once the latter has reflected at the bottom and is directed upward (between $x = -120$ and -55 km); in this trajectory the main beam looks therefore slightly different from the winter case.

The main beam itself encounters the thermocline near $x = -120$ km. In winter, the beam reflects at the surface without undergoing any distortion (Fig. 7C), but in Fig. 7A the pronounced variation in stratification in the seasonal thermocline causes internal (or secondary) reflections, hence scattering and a severe distortion of the beam. In the presence of nonlinear and non-hydrostatic effects (both are however absent in the present model), the local disturbance of the seasonal thermocline provoked by the incoming beam can give rise to the appearance of internal solitary waves (Gerkema, 2001). For the Bay of Biscay, this phenomenon has been reported in the literature (New and Pingree, 1990, 1992). In these studies the connection with the main beam was established: in the central Bay of Biscay internal solitary waves occur precisely where the main beam encounters the thermocline (near

$x = -120$ km in Fig. 7A). Moreover, they are indeed observed only during summer (New and Da Silva, 2002).

In the region of scattering, relatively much energy remains temporarily behind in and above the thermocline, as the spots of strong tidal currents show. This is more clearly shown in an enlargement, see Fig. 8. In the upper 60 m, phase propagation is predominantly horizontal (Fig. 8B); in this respect the behaviour resembles that of a pure interfacial tide in a two-layer system (with thin upper layer d). The phase speed in such a system is given by $c^2 = g'd$; representative values are $g' = 0.01 \text{ m s}^{-2}$ and $d = 60$ m. One finds a wavelength of about 35 km, which corresponds well to the wavelength in the upper 60 m in

Fig. 8B, and is also fairly close to the observed value of 40–45 km (New and Da Silva, 2002). Yet, the internal tide here differs crucially from an interfacial tide: for the latter, one would find a *constant* amplitude A in the upper layer, which obviously is not the case in Fig. 8A. Instead of a constant amplitude, one observes the spots referred to above, formed by an occasional constructive superposition of the modes, in the absence of a distinct interfacial mode.

5. Discussion

The numerical results presented in Section 3.2 show that there are two main well-separated regions of internal-tide generation: one in the seasonal thermocline, and a deeper seasonally independent one (between 300 and 900 m depth). The latter dominates the integrated conversion rate; seasonal influences are, therefore, of secondary importance. This qualitative conclusion can be expected to remain valid if one would include factors ignored here, like three-dimensionality and nonlinearity. The possible importance of three-dimensional features like canyons was stressed by Munk (1997), but for the region considered here they are not likely to change the conversion rate dramatically, because the cross-slope barotropic tidal flux (Q_0) exceeds the along-slope one (see Fig. 1). Nonlinear effects and mixing would locally change the stratification and hence the conversion rates; for example, Xing and Davies (1998) found an increase by a factor three. (The caveat concerning artificial mean fields should be noticed when evaluating conversion rates in the nonlinear problem, see Section 3.)

The integrated conversion rates we found in Section 3.2 (for realistic topography and stratification) exceed those obtained by Baines (1982) by one order of magnitude. Even if we adopt his setting (linear slope and constantly stratified deep layer, Section 3.1), we still find values much higher than his: one order of magnitude higher for the Bay of Biscay as a whole, two orders of magnitude for the location under consideration. (Baines probably used a barotropic cross-slope flux that

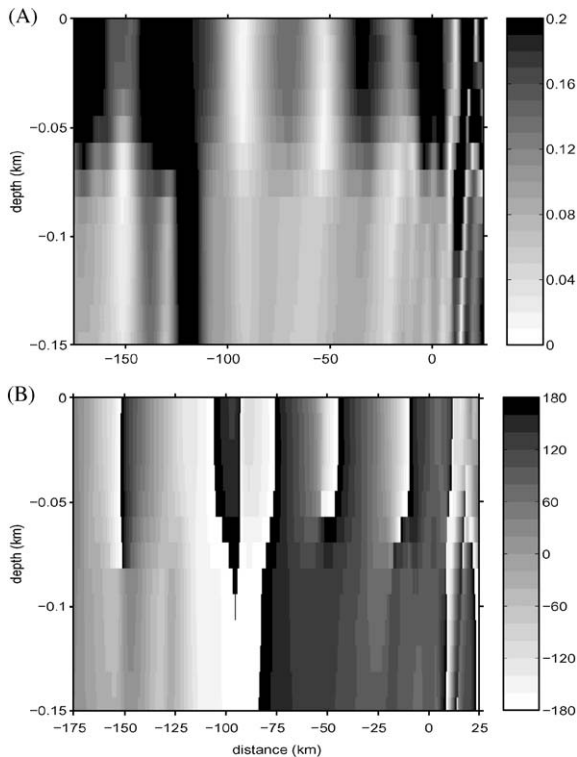


Fig. 8. Model results, upper layer during summer (enlargement of Fig. 7(A, B): the baroclinic cross-slope component, decomposed into: (A) amplitude A (in m s^{-1}); and (B) phase ϕ (in degrees; notice that the extremes of black and white denote the same phase).

is much weaker than the observed value.) In the setting with a linear slope, we verified our model results by comparing them with the exact theoretical result for a step-topography (Fig. 4).

Unfortunately, at this stage it is difficult to verify the conversion rates empirically. Recent developments in the use of Topex/Poseidon satellite observations bear the promise of providing accurate conversion rates sometime in the near future. At present the estimated rates are probably already reasonable in a globally integrated sense (Egbert and Ray, 2000), but still uncertain for individual locations. In situ measurements and an assessment of the energy fluxes (not yet carried out in the Bay of Biscay) would provide a much needed test for theoretical and numerical models.

Although the total energy involved in the internal tides here shows little seasonal dependence, their evolution and propagation changes much with the seasons. First of all, the extra source-region in the seasonal thermocline, though relatively small, gives rise to internal-tide currents in the upper layer at the ocean-side (clearly visible in the observations, too), and to internal tides propagating on-shelf. The dynamics of the main beam, whose generation is not affected by the seasons, shows a marked seasonal dependence too, but not before it approaches the surface in the central part of the Bay. During winter, the beam continues its propagation undisturbed after the reflection at the surface; during summer, it gets severely distorted due to scattering in the seasonal thermocline. As discussed above, this process of scattering can be linked to the occurrence of internal solitary waves.

Acknowledgements

The authors are much indebted to H.M. van Aken, who designed and supervised the field program, and to S. Ober and C. Veth for their assistance with the ADCP observations. T.G. and L.R.M.M. received financial support from the project INTAS01-0025.

References

- Baines, P.G., 1982. On internal tide generation models. *Deep-Sea Research* 29, 307–388.
- Brekhovskikh, L.M., 1960. *Waves in Layered Media*. Academic Press, New York.
- DeWitt, L.M., Levine, M.D., Paulson, C.A., Burt, W.V., 1986. Semidiurnal internal tide in JASIN: observations and simulation. *Journal of Geophysical Research* 91 (C2), 2581–2592.
- Durran, D.R., 1999. *Numerical Methods for Wave Equations in Geophysical Fluid Dynamics*. Springer, Berlin.
- Egbert, G.D., Ray, R.D., 2000. Significant dissipation of tidal energy in the deep ocean inferred from satellite altimeter data. *Nature* 405, 775–778.
- Gerkema, T., 2001. Internal and interfacial tides: beam scattering and local generation of solitary waves. *Journal of Marine Research* 59, 227–255.
- Gerkema, T., 2002. Application of an internal-tide generation model to baroclinic spring-neap cycles. *Journal of Geophysical Research* 107 10.1029/2001JC001177.
- Khatiwala, S., 2003. Generation of internal tides in an ocean of finite depth: analytical and numerical calculations. *Deep-Sea Research* 50 (I), 3–21.
- Lam, F.P.A., Maas, L.R.M., Gerkema, T., 2004. Spatial structure of tidal and residual currents as observed over the shelf break in the Bay of Biscay. *Deep-Sea Research* 51 (8), 1075–1096.
- LeBlond, P.H., Mysak, L.A., 1978. *Waves in the Ocean*. Elsevier Oceanography Series. Elsevier, Amsterdam.
- LeCann, B., 1990. Barotropic tidal dynamics of the Bay of Biscay shelf: observations, numerical modelling and physical interpretation. *Continental Shelf Research* 10 (8), 723–758.
- Llewellyn Smith, S.G., Young, W.R., 2002. Conversion of the barotropic tide. *Journal of Physical Oceanography* 32, 1554–1566.
- Morozov, E.G., 1995. Semidiurnal internal wave global field. *Deep-Sea Research* 42 (1), 135–148.
- Munk, W., 1997. Once again: once again—tidal friction. *Progress in Oceanography* 40 (1–4), 7–35.
- New, A.L., Da Silva, J.C.B., 2002. Remote-sensing evidence for the local generation of internal soliton packets in the central Bay of Biscay. *Deep-Sea Research* 49, 915–934.
- New, A.L., Pingree, R.D., 1990. Large-amplitude internal soliton packets in the central Bay of Biscay. *Deep-Sea Research* 37, 513–524.
- New, A.L., Pingree, R.D., 1992. Local generation of internal soliton packets in the central Bay of Biscay. *Deep-Sea Research* 39 (9), 1521–1534.
- Pingree, R.D., Mardell, G.T., New, A.L., 1986. Propagation of internal tides from the upper slopes of the Bay of Biscay. *Nature* 321, 154–158.
- Pingree, R.D., New, A.L., 1991. Abyssal penetration and bottom reflection of internal tidal energy into the Bay of Biscay. *Journal of Physical Oceanography* 21 (1), 28–39.

- Sanchis, A., 2003. Modélisation de la marée interne: méthode analytique et validation numérique. MSc, Thesis, Ecole Centrale de Nantes.
- Sjöberg, B., Stigebrandt, A., 1992. Computations of the geographical distribution of the energy flux to mixing processes via internal tides and the associated vertical circulation in the ocean. *Deep-Sea Research* 39 (2), 269–291.
- St. Laurent, L., Stringer, S., Garrett, C., Perrault-Joncas, D., 2003. The generation of internal tides at abrupt topography. *Deep-Sea Research* 50, 987–1003.
- Van Aken, H.M., 1995. Biscay 1993. Cruise Report, Netherlands Institute for Sea Research (NIOZ).
- Van Aken, H.M., 2001. The hydrography of the mid-latitude. Northeast Atlantic Ocean Part III: The thermocline water masses. *Deep-Sea Research* 48 (I), 237–267.
- Xing, J., Davies, A.M., 1998. Formulation of a three-dimensional shelf edge model and its application to internal tide generation. *Continental Shelf Research* 18, 405–440.